Nearly Total Solar Absorption in Ultrathin Nanostructured Iron Oxide for Efficient Photoelectrochemical Water Splitting

Ken Xingze Wang,[†] Zongfu Yu,[‡,∥] Victor Liu,[‡,#] Mark L. Brongersma,[§] Thomas F. Jaramillo,[⊥] and Shanhui Fan*,[‡]

[†]Department of Applied Physics, Stanford University, Stanford, California 94305, United States
[‡]Department of Electrical Engineering, Stanford University, Stanford, California 94305, United States
[§]Department of Materials Science and Engineering, Stanford University, Stanford, California 94305, United States
[⊥]Department of Chemical Engineering, Stanford University, Stanford, California 94305, United States

ABSTRACT: We demonstrate using first-principles full-field electromagnetic simulations that nearly total above-band-gap solar absorption can be achieved in ultra-thin-film iron oxide photoanodes for water splitting applications. In our designed structure, all regions of iron oxide are away from the interface between iron oxide and water by a distance of less than the hole diffusion length, which is assumed to be 20 nm in our simulation. The absorption in our structure corresponds to a photocurrent density of 12.5 mA/cm^2 if one assumes an air mass 1.5 solar spectrum and a unity absorbed photon-to-current efficiency. Our photon management strategy eliminates the trade-off between optical absorption and carrier collection as commonly found in conventional designs and is generally applicable to photoelectrochemical cells.

KEYWORDS: photon management, antireflection, light trapping, nanocone, hematite, photoelectrochemical cells
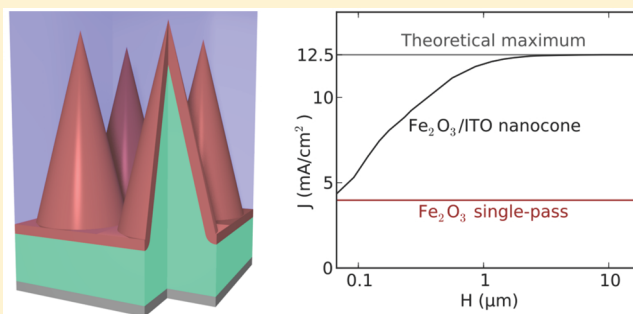
Hematite (α-iron oxide) is a promising material for the photoelectrochemical conversion of sunlight to fuel.[1−8] It is inexpensive, abundant, nontoxic, and stable.[9] Its band gap of around 2.1 eV is near optimal for water splitting by a single semiconductor from a voltage perspective.[1,10,11] If every above-band-gap photon absorbed can contribute to water splitting, a hematite photoanode could generate a theoretical maximum current of 12.5 mA/cm^2 under the air mass 1.5 solar spectrum.[12,13]

However, in practice, hematite photoanodes produce photocurrents far lower than the theoretical maximum of 12.5 mA/cm^2. This is due in large part to the extremely short diffusion length of charge carriers.[9,14,15] As a result, it is mostly the sunlight absorbed within a very thin, nanoscale layer of hematite near the hematite−water interface that can contribute to water splitting, which severely limits the efficiency of such photoelectrochemical cells. A number of approaches have been carried out to maximize absorption in hematite, such as stacking multiple layers in tandem,[16−22] porous thin films,[23−29] nanostructured arrays,[30−42] and plasmonics.[43−50] None of these approaches has yet to reach complete absorption in a hematite photoanode.

In this work, we seek to overcome this difficulty by considering an appropriate optical design for a hematite photoanode as shown in Figure 1, which consists of a nanoscale hematite layer coated on a nanocone array made of a transparent conducting oxide. At the front face of the hematite layer is the water interface. Hematite has a hole diffusion length in the range of 2 to 20 nm.[14,15] In our calculation, we assume a hole diffusion length of 20 nm, which is within reasonable experimental range. Under the assumption and with the choice of d = 20 nm for our film thickness, no regions of hematite are more than 20 nm from the water−hematite interface, satisfying electronic considerations in terms of carrier diffusion. Using optical simulations, we show that such a structure enables near-complete absorption of above-band-gap light, which corresponds to a nearly ideal photocurrent of 12.5 mA/cm^2, if one assumes that within the minority carrier diffusion length every generated carrier is collected. In general, the values of current density quoted in this paper are obtained by assuming such a unity absorbed photon-to-current efficiency (APCE),[13] as the film thickness is kept to be less than the hole diffusion length. These values should only be interpreted as a convenient measure of the optical absorption efficiency of the structure. Quoting these values is useful when one needs to compare optical properties of different structures. Actual photocurrent achievable in any structure results from both optical absorption and carrier separation and collection, and the latter can be significantly more complex than the simplified assumption here.

Our design here is motivated by the powerful concept of orthogonalizing the directions of photon propagation and
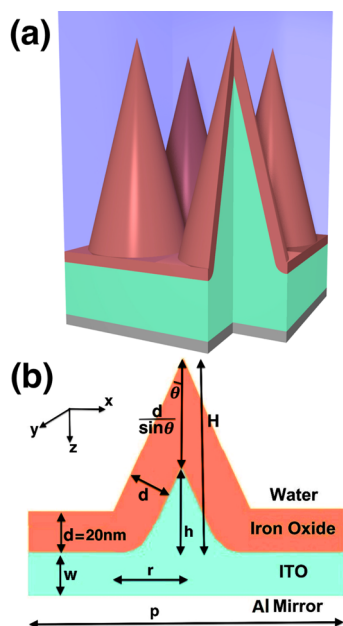
Figure 1. Core−shell nanocone array. (a) Three-dimensional view of the right circular cones forming a square lattice on the substrate. (b) Vertical cross section through the apex showing the ITO core and the hematite shell. The bottom part of the hematite shell is rounded to ensure that any location of hematite is within 20 nm from the hematite−water interface.

charge carrier transport, as discussed in refs 51−55. There has been at least one experimental exploration of the core−shell geometry similar to our design.[56] With conventional design, there is a trade-off between absorption and carrier collection efficiency. A thinner structure has better collection efficiency but suffers from weaker absorption. The main contribution of our paper is to show that this trade-off can in fact be eliminated with optical design and that complete optical absorption can be accomplished in an ultrathin structure. Our work therefore removes one of the roadblocks for reaching the theoretical upper limit for photocurrent in water splitting.

We start by briefly reviewing the two separate electronic considerations in hematite photoanodes that lead to the design of Figure 1. In the structure of Figure 1, incoming sunlight generates electron−hole pairs. The holes then diffuse to the water−hematite interface in order to enable water splitting, while the electrons diffuse toward the transparent conducting oxide support. The electrons are the majority carrier and are much more mobile than the holes,[14,15,57,58] and the electron diffusion length should be significantly greater than all the length scales considered in this paper. It follows that any region of hematite should not be farther away from the hematite−water interface by more than the hole diffusion length. The need for efficient carrier extraction therefore favors thin hematite films. On the other hand, a built-in electric field is required to facilitate carrier transport. Therefore the thickness of the hematite film should not be less than the thickness of the space charge region and certainly cannot be arbitrarily small.[59] Considering both electronic considerations, our optical design seeks to maximize optical absorption in a hematite thin film structure where any region of the hematite is within 20 nm of the nearest hematite−water interface. Although charge transport is very complex in hematite,[60−65] we assume that all photogenerated carriers in such a design for hematite can

contribute to the photocurrent, a simplification that allows us to focus on the optical aspects of our structure. We note that, depending on the preparation conditions, hematite can have vastly different electronic properties, and the choice of the 20 nm value is within the range of hole diffusion lengths found in the literature.[14,15] The concept of our optical design, however, is independent of this particular numerical value. One can similarly obtain near-unity absorption characteristics with thinner structures.

We now discuss our photonic design considerations. The first consideration in our design is to achieve light trapping by orthogonalizing the photon propagation and carrier transport and by packing as much hematite as possible in a given volume or area of the device, while satisfying the aforementioned electronic considerations. Certainly, the amount of absorption scales with the volume of hematite, but electronic considerations require hematite thin films with thicknesses less than the hole diffusion length. Thus, to design an effective absorber, one would like to closely pack the nanostructures in the array while increasing the aspect ratio of individual nanostructures. This necessitates the type of core−shell structure that is shown in Figure 1.

The second photonic consideration is to achieve antireflection, which is necessary since the refractive index of hematite is much higher than that of water. Traditional antireflection coatings require an additional layer between the hematite and water, which would impede the water splitting process, and fortunately, tapering of nanostructures, which provides a graded index for optical impedance matching, has proven to be an effective antireflection strategy.[66,67] In Figure 1, as the radius of the nanocone cross section increases from zero to the maximum at the base, the effective (spatially averaged) refractive index undergoes a continuous transition from the refractive index of water to that of the hematite. There are two geometric requirements for effective antireflection which we incorporate into our design. First, the nanocone lattice periodicity needs to be much smaller than the wavelength of incoming light to appear as an effectively averaged refractive index. Second, the height of the nanocone needs to be large enough for a smooth transition. Satisfying these two requirements should result in strong suppression of reflection over broad ranges of both wavelengths and incident angles, a desirable characteristic to enable strong solar absorption at any time of day. Fortunately, both photonic considerations can be satisfied by the tapered core−shell structure. We expect better performance from taller nanocones, which is confirmed by our results. Later, we show that the strategies are so effective that the aspect ratio need not be extreme to achieve nearly complete sunlight absorption.

To satisfy the electronic and photonic considerations discussed above, we employ the class of structures shown in Figure 1, which consists of a square lattice of core−shell nanocones. These structures sit atop an aluminum mirror, where an indium tin oxide (ITO) layer serves as a substrate for electron collection, and the hematite is conformally deposited onto the ITO substrate. The electrolyte is assumed to have the same optical constants as water. We smooth the bottom of the ITO cone, and as a result, any location within hematite is always within 20 nm of the nearest hematite−water interface.

Given the geometric arrangement in Figure 1 and maintaining the hematite thickness at $d = 20$ nm, we now optimize its optical absorption. The structure is uniquely determined by four parameters: the periodicity of the square

lattice p, the base radius of the hematite nanocone r, the height of the ITO nanocone h, and the thickness of the planar ITO layer w. Once the structure is defined, we run full-field electromagnetic simulations to calculate the normal incidence absorption spectrum corresponding to the usable solar spectrum ranging from 280 to 591 nm,[68,69] and we integrate over this range to calculate the photocurrent density

$$J = \frac{e}{2\pi\hbar c} \int_{280nm}^{591nm} \text{AM1.5}(\lambda) \; \text{absorption}(\lambda) \; \lambda \; d\lambda$$

generated from the absorption in hematite, excluding the absorption in any other materials. In the frequency domain simulations, we use experimental values of complex dielectric constants for the four materials in the device: water, hematite, ITO, and aluminum.[70,71]

We adjust the four parameters p, r, h, and w (labeled in Figure 1 and defined in Table 1) to search for a global

Table 1. Nomenclature: These Geometric Parameters Are Labeled in Figure 1

parameter	definition, formula, and/or value
d	thickness of the hematite film; $d = 20$ nm for all structures shown in this paper
r	radius of the hematite cone
p	periodicity of the square lattice
h	height of the ITO cone
w	thickness of the planar layer of the ITO substrate; $w = 100$ nm for all structures shown in this paper
θ	half of the apex angle of the cones; $\theta = \sin^{-1}\{[r(r^2 + h^2 - 2hd)^{1/2} - d(h - d)]/[(h - d)^2 + r^2]\}$
H	total height of the hematite layer from the tip of the hematite cone to the bottom of the planar hematite film; $H = h + d/\sin\theta$

maximum of photocurrent. We find that the periodicity p should be small in order to closely pack as many nanocones as possible, with $p = 60$ nm leading to high photocurrents, as the hematite nanocone should fully utilize the space within the unit cell with a base radius of $r = 30$ nm. The ITO substrate does not play an important role in the overall performance, and we assign a moderate value of $w = 100$ nm, which is sufficient for electrical conductance.[72,73] The photocurrent converges to the maximum value of 12.5 mA/cm² as the height h increases, and we plot in Figure 2a the relationship between the absorption spectra and the total heights $H = h + t/\sin\theta$, where θ is half of the apex angle of the cone. At a total height of $H = 3$ μm, or approximately $h = 1$ μm, the absorption coefficient remains near unity across the spectrum above the hematite band gap.

The near-perfect photocurrent indicates very effective antireflection in the core−shell nanostructure. With sufficiently tall nanocones, the high aspect ratio ensures a smooth transition of refractive indices and provides excellent optical impedance matching between the tip and the bottom of the nanocones, in other words, between water and hematite layers. In Figure 3a, we plot the absorption density, which is the product of the imaginary part of the dielectric constant and the electric field intensity, for a normally incident wavelength of 300 nm and a nanostructure with the said p, r, and w values and with $h = 200$ nm and therefore $H = 600$ nm. The absorption is nearly complete, and we observe in Figure 3a that all photons are absorbed in hematite due to the effective antireflection. The corresponding absorption spectrum for this particular structure is plotted in Figure 2a. For the same structure at a longer wavelength of 500 nm, we again plot the absorption density in
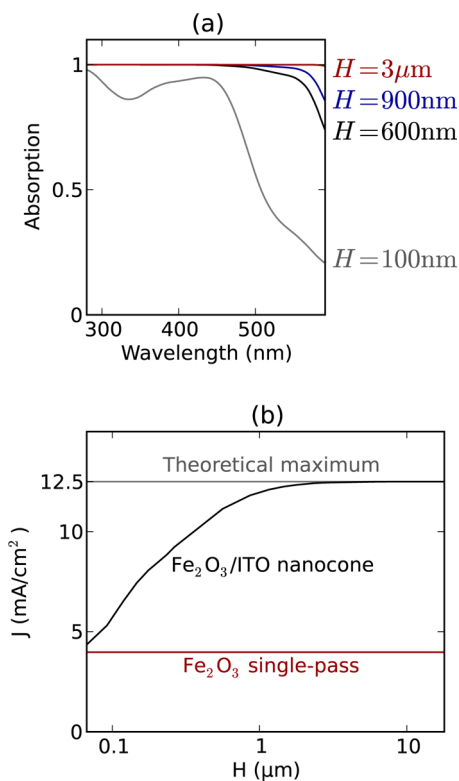

Figure 2. Results from full-field simulations. (a) Absorption spectra for the structure with different heights, with all other parameters being equal. Note that this absorption includes only the absorption within the hematite layer; that is, any absorption loss in ITO or back mirror has been excluded but not neglected. (b) Photocurrent generated by the structure with a range of heights, compared to the single-pass photocurrent. Since only the photons generated within the first 20 nm layer of the planar hematite film can contribute to the photocurrent, the single-pass photocurrent remains flat regardless of the actual structure thickness.

Figure 3b. Although the antireflection is almost equally effective, due to the relatively weak absorptivity of hematite at this wavelength, more light penetrates into the bottom part of the hematite nanocone and excites slot waveguide modes between the nanocones.

In Figure 2b, we compare the performance of our structure at different total heights H to the photocurrent J generated from single-pass absorption through hematite at thicknesses equal to H. In the planar structure with single-pass absorption, we assume perfect antireflection at the water−hematite interface; however, due to the extremely short hole diffusion length of 20 nm, only the photons absorbed in the first 20 nm region in the hematite can effectively contribute to the photocurrent. On the other hand, in the nanocone structure, all absorption in hematite occurs within 20 nm from the water−hematite interface, and hence all photons can, in principle, contribute, resulting in a much higher photocurrent.

We can estimate the relative contributions of the two photonic considerations. Orthogonalization raises the absorption from single-pass absorption of a flat film with a thickness equal to the hole diffusion length of 20 nm, with a photocurrent of 4 mA/cm², to near unity shown in Figure 2b, and the relative improvement is 68%. Antireflection reduces the reflection at the water−hematite interface, which is approximately 15% of the incident sunlight.
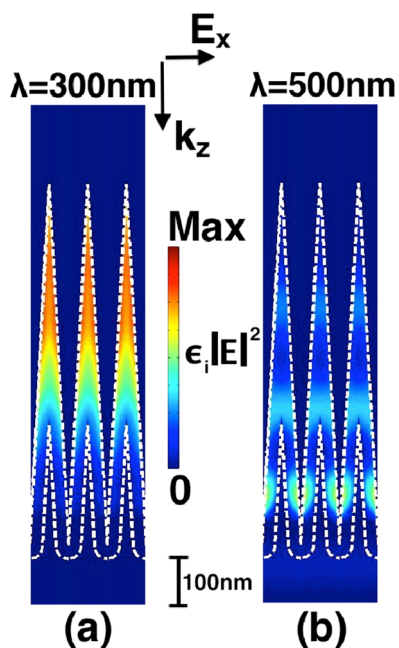
Figure 3. Absorption profiles for a sample structure. (a) Vertical slice at a free space wavelength of $\lambda = 300$ nm. (b) The same vertical slice at a free space wavelength of $\lambda = 500$ nm. The white dashed lines indicate the position of material interfaces, separating water, hematite, and ITO from top to bottom. The normally incident light is polarized in-plane. The blue color represents low absorption intensity, and the red color represents high absorption intensity, as indicated by the color bar between the subfigures. The periodicity p is 60 nm, and the total height H is 522 nm. The tip of the cone is kept sharp, but the bottom is rounded to make sure that holes can transport to the water−hematite interface.

Although we focus on circular cones to demonstrate our strategy, the same principles apply to other tapering structures, for example, pyramids or inverted pyramids. In Figure 4, we calculate the absorption spectra for these three different geometries. All three structures have the same material composition and geometric parameters; in particular, the total height of the structures, $H = 264$ nm, as well as the height of the ITO core and the thickness of the hematite shell, are kept the same. The square lattices are identical with a spacing of $p = 60$ nm. The thickness of the hematite layer is always kept at $d = 20$ nm in the same manner as Figure 1b to ensure hole transport. It is important to note that, for any of the structures in Figure 4, nearly complete absorption across the entire spectrum above the hematite band gap can be achieved at sufficiently high aspect ratios, similar to the trend in Figure 2. Even when the heights are not sufficient for complete absorption, the results in Figure 4 reinforce the effectiveness of our approach. On one hand, at shorter wavelengths, the cone and pyramid structures provide better antireflection than the inverted pyramid structure because the tips bring better impedance matching than the ridges. On the other hand, at longer wavelengths, the pyramid structure absorbs better than the cone, and the inverted pyramid structure performs even better, because we are able to pack more hematite given the geometric constraints. More specifically, due to the larger base area of the pyramid than the cone, the hematite shell in the pyramid structure occupies a larger volume than in the cone structure; because more surface area is exposed in an inverted
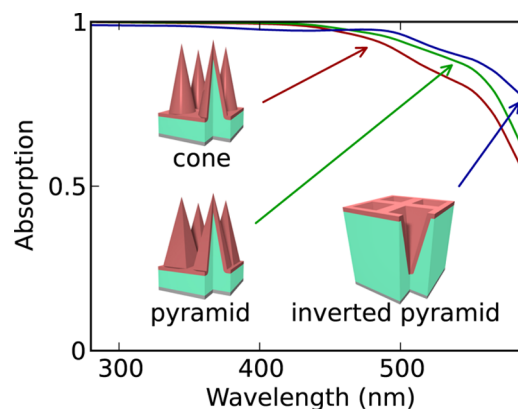

Figure 4. Absorption spectra for the three different structures with the same total height $H = 264$ nm and identical square lattice with periodicity $p = 60$ nm. Each of the structures contains the same materials, including hematite and ITO, as sketched in Figure 1. In each case, the bottom part of the hematite shell is rounded, and as a result, the thickness of the hematite layer is always kept at $d = 20$ nm for hole transport. To avoid confusion, we emphasize that the tip of the hematite cone does not need to be rounded because of the large diffusion length of electrons; in practice, the sharp tip is not required because the design strategy is broadband and tolerates slight variations of the structures. The red, green, and blue curves correspond to the absorption spectra of the nanoscale cone, pyramid, and inverted pyramid structures, respectively.

structure, an inverted pyramid structure accommodates more hematite than the corresponding pyramid structure.

The nanostructure designed in this study could be fabricated using a variety of techniques, such as atomic layer deposition,[59,74,75] etching,[76−79] and atmospheric pressure chemical vapor deposition.[25,56,80,81] We note that mass transport issues have not been a problem in previous studies.[82] Additionally, we expect that the large surface area is likely sufficient to assist catalysis without causing major problems with surface recombination.[83] Given the broadband nature of our strategies, the performance of the nanostructures in Figure 4 should be robust against slight variations in fabrication; for example, the sharp tip of the conic structures is not required to achieve near-perfect antireflection. While it is important to experimentally explore other practical issues, the light management strategies are general for photoelectrochemical cells.

■ AUTHOR INFORMATION

Corresponding Author
*E-mail: shanhui@stanford.edu.

Present Addresses
‖Department of Electrical and Computer Engineering, University of Wisconsin−Madison, Madison, Wisconsin 53706, United States.
#Palo Alto Research Center (PARC), 3333 Coyote Hill Road, Palo Alto, California 94304, United States.

Notes
The authors declare no competing financial interest.

■ ACKNOWLEDGMENTS

■ REFERENCES

(1) van de Krol, R., Grätzel, M., Eds. *Photoelectrochemical Hydrogen Production*; Springer: Berlin, 2012.

(2) Fujishima, A.; Honda, K. Electrochemical photolysis of water at a semiconductor electrode. *Nature* **1972**, *238*, 37−38.

(3) Grätzel, M. Photoelectrochemical cells. *Nature* **2001**, *414*, 338−344.

(4) Zou, Z.; Ye, J.; Sayama, K.; Arakawa, H. Direct splitting of water under visible light irradiance with an oxide semiconductor photocatalyst. *Nature* **2001**, *414*, 625.

(5) Lewis, N. S.; Nocera, D. G. Powering the planet: chemical challenges in solar energy utilization. *Proc. Natl. Acad. Sci. U.S.A.* **2006**, *103*, 15729−15735.

(6) Chen, X.; Shen, S.; Guo, L.; Mao, S. S. Semiconductor-based photocatalytic hydrogen generation. *Chem. Rev.* **2010**, *110*, 6503.

(7) Walter, M. G.; Warren, E. L.; McKone, J. R.; Boettcher, S. W.; Mi, Q.; Santori, E. A.; Lewis, N. S. Solar water splitting cells. *Chem. Rev.* **2010**, *110*, 6446−6473.

(8) Haussener, S.; Xiang, C.; Spurgeon, J. M.; Ardo, S.; Lewis, N. S.; Weber, A. Z. Modeling, simulation, and design criteria for photoelectrochemical water-splitting systems. *Energy Environ. Sci.* **2012**, *5*, 9922.

(9) Sivula, K.; Formal, F. L.; Grätzel, M. Solar water splitting: progress using hematite (α-Fe$_2$O$_3$) photoelectrodes. *Chem. Sus. Chem.* **2011**, *4*, 432−449.

(10) Marusak, L. A.; Messier, R.; White, W. B. Optical absorption spectrum of hematite, α-Fe$_2$O$_3$ near IR to UV. *J. Phys. Chem. Solids* **1980**, *41*, 981−984.

(11) Gilbert, B.; Frandsen, C.; Maxey, E. R.; Sherman, D. M. Bandgap measurement of bulk and nanoscale hematite by soft x-ray spectroscopy. *Phys. Rev. B* **2009**, *79*, 035108.

(12) Bird, R. E.; Hulstrom, R. L.; Lewis, L. J. Terrestrial solar spectral data sets. *Solar Energy* **1983**, *30*, 563.

(13) Chen, Z.; Jaramillo, T. F.; Deutsch, T. G.; Kleiman-Schwarsctein, A.; Forman, A. J.; Gaillard, N.; Garland, R.; Takanabe, K.; Heske, C.; Sunkara, M.; McFarland, E. W.; Domen, K.; Miller, E. L.; Turner, J. A.; Dinh, H. N. Accelerating materials development for photoelectrochemical hydrogen production: standards for methods, definitions, and reporting protocols. *J. Mater. Res.* **2010**, *25*, 3−16.

(14) Kennedy, J. H.; Frese, K. W. Photooxidation of water at α-Fe$_2$O$_3$ electrodes. *J. Electrochem. Soc.* **1978**, *125*, 709.

(15) Dare-Edwards, M. P.; Goodenough, J. B.; Hamnett, A.; Trevellick, P. R. Electrochemistry and photoelectrochemistry of iron (III) oxide. *J. Chem. Soc., Faraday Trans.* **1983**, *1* (79), 2027.

(16) Itoch, K.; Bockris, J. O. Thin film photoelectrochemistry: iron oxide. *J. Electrochem. Soc.* **1984**, *131*, 1266−1271.

(17) Khaselev, O.; Turner, J. A. A monolithic photovoltaic-photoelectrochemical device for hydrogen production via water splitting. *Science* **1998**, *280*, 425.

(18) Alexander, B. D.; Kulesza, P. J.; Rutkowska, L.; Solarska, R.; Augustynski, J. Metal oxide photoanodes for solar hydrogen production. *J. Mater. Chem.* **2008**, *18*, 2298−2303.

(19) van de Krol, R.; Liang, Y. Q.; Schoonman, J. Solar hydrogen production with nanostructured metal oxides. *J. Mater. Chem.* **2008**, *18*, 2311−2320.

(20) Minggu, L. J.; Daud, W. R. W.; Kassim, M. B. An overview of photocells and photoreactors for photoelectrochemical water splitting. *Int. J. Hydrogen Energy* **2010**, *35*, 5233−5244.

(21) Tilley, S. D.; Cornuz, M.; Sivula, K.; Grätzel, M. Light-induced water splitting with hematite: improved nanostructure and iridium oxide catalysis. *Angew. Chem.* **2010**, *122*, 6549−6552.

(22) Brillet, J.; Yum, J.-H.; Cornuz, M.; Hisatomi, T.; Solarska, R.; Augustynski, J.; Grätzel, M.; Sivula, K. Highly efficient water splitting by a dual-absorber tandem cell. *Nat. Photonics* **2012**, *6*, 824.

(23) Bjorksten, U.; Moser, J.; Grätzel, M. Photoelectrochemical studies on nanocrystalline hematite films. *Chem. Mater.* **1994**, *6*, 858−863.

(24) Rodriguez, I.; Atienzar, P.; Ramiro-Manzano, F.; Meseguer, F.; Corma, A.; Garcia, H. Photonic crystals for applications in photoelectrochemical processes solar cells with inverse opal topology photonics and nanostructures. *Photonics Nanostruct. Fundam. Appl.* **2005**, *3*, 148−154.

(25) Kay, A.; Cesar, I.; Grätzel, M. New benchmark for water photooxidation by nanostructured α-Fe$_2$O$_3$ films. *J. Am. Chem. Soc.* **2006**, *128*, 15714−15721.

(26) Rodriguez, I.; Ramiro-Manzano, F.; Atienzar, P.; Martinez, J. M.; Meseguer, F.; Garcia, H.; Corma, A. Solar energy harvesting in photoelectrochemical solar cells. *J. Mater. Chem.* **2007**, *17*, 3205−3209.

(27) Ramiro-Manzano, F.; Atienzar, P.; Rodriguez, I.; Meseguer, F.; Garcia, H.; Corma, A. Apollony photonic sponge based photoelectrochemical solar cells. *Chem. Commun.* **2007**, 242−244.

(28) Hu, Y.-S.; Kleiman-Shwarsctein, A.; Forman, A. J.; Hazen, D.; Park, J.-N.; McFarland, E. W. Pt-doped α-Fe$_2$O$_3$ thin films active for photoelectrochemical water splitting. *Chem. Mater.* **2008**, *20*, 3803−3805.

(29) Brillet, J.; Grätzel, M.; Sivula, K. Decoupling feature size and functionality in solution-processed, porous hematite electrodes for solar water splitting. *Nano Lett.* **2010**, *10*, 4155−4160.

(30) Boettcher, S. W.; Warren, E. L.; Putnam, M. C.; Santori, E. A.; Turner-Evans, D.; Kelzenberg, M. D.; Walter, M. G.; McKone, J. R.; Brunschwig, B. S.; Atwater, H. A.; Lewis, N. S. Photoelectrochemical hydrogen evolution using Si microwire arrays. *J. Am. Chem. Soc.* **2011**, *133*, 1216−1219.

(31) Mao, A.; Han, G. Y.; Park, J. H. Synthesis and photoelectrochemical cell properties of vertically grown α-Fe$_2$O$_3$ nanorod arrays on a gold nanorod substrate. *J. Mater. Chem.* **2010**, *20*, 2247−2250.

(32) Ling, Y.; Wang, G.; Wheeler, D. A.; Zhang, J. Z.; Li, Y. Sn-doped hematite nanostructured for photoelectrochemical water splitting. *Nano Lett.* **2011**, *11*, 2119−2125.

(33) Deng, J.; Zhong, J.; Pu, A.; Zhang, D.; Li, M.; Sun, X.; Lee, S.-T. Ti-doped hematite nanostructures for solar water splitting with high efficiency. *J. Appl. Phys.* **2012**, *112*, 084312.

(34) Dasgupta, N. P.; Yang, P. Semiconductor nanowires for photovoltaic and photoelectrochemical energy conversion. *Front. Phys.* **2013**, *2095−0462*, 1−14.

(35) Kim, J. Y.; Magesh, G.; Youn, D. H.; Jang, J.-W.; Kubota, J.; Domen, K.; Lee, J. S. Single-crystalline, wormlike hematite photoanodes for efficient solar water splitting. *Sci. Rep.* **2013**, *3*, 2681.

(36) Cho, I. S.; Lee, C. H.; Feng, Y.; Logar, M.; Rao, P. M.; Cai, L.; Kim, D. R.; Sinclair, R.; Zheng, X. Codoping titanium dioxide nanowires with tungsten and carbon for enhanced photoelectrochemical performance. *Nat. Commun.* **2013**, *4*, 1723.

(37) Fu, Y.; Chen, J.; Zhang, H. Synthesis of Fe$_2$O$_3$ nanowires by oxidation of iron. *Chem. Phys. Lett.* **2001**, *350*, 491−494.

(38) Fan, Z.; Wen, X.; Yang, S.; Lu, J. G. Controlled *p*- and *n*-type doping of Fe$_2$O$_3$ nano belt field effect transistors. *Appl. Phys. Lett.* **2005**, *87*, 013113.

(39) Park, J. H.; Kim, S.; Bard, A. J. Novel carbon-doped TiO$_2$ nanotube arrays with high aspect ratios for efficient solar water splitting. *Nano Lett.* **2006**, *6*, 24−28.

(40) Yu, T.; Zhu, Y.; Xu, X.; Yeong, K.-S.; Shen, Z.; Chen, P.; Lim, C.-T.; Thong, J. T.-L.; Sow, C.-H. Substrate-friendly synthesis of metal oxide nanostructures using a hotplate. *Small* **2006**, *2*, 80−84.

(41) Peng, L.; Xie, T.; Fan, Z.; Zhao, Q.; Wang, D.; Zheng, D. Surface photovoltage characterization of an oriented α-Fe$_2$O$_3$ nanorod array. *Chem. Phys. Lett.* **2008**, *459*, 159−163.

(42) Beermann, N.; Vayssieres, L.; Lindquist, S.-E.; Hagfeldt, A. Photoelectrochemical studies of oriented nano rod thin films of hematite. *J. Electrochem. Soc.* **2000**, *147*, 2456−2461.

(43) Schuller, J. A.; Barnard, E. S.; Cai, W.; Jun, Y. C.; White, J. S.; Brongersma, M. L. Plasmonics for extreme light concentration and manipulation. *Nat. Mater.* **2010**, *9*, 193.

(44) Liu, Z.; Hou, W.; Pavaskar, P.; Aykol, M.; Cronin, S. B. Plasmon resonant enhancement of photocatalytic water splitting under visible illumination. *Nano Lett.* **2011**, *11*, 1111−1116.

(45) Thomann, I.; Pinaud, B. A.; Chen, Z.; Clemens, B. M.; Jaramillo, T. F.; Brongersma, M. L. Plasmon enhanced solar-to-fuel energy conversion. *Nano Lett.* **2011**, *11*, 3440−3446.

(46) Warren, S. C.; Thimsen, E. Plasmonic solar water splitting. *Energy Environ. Sci.* **2012**, *5*, 5133−5146.

(47) Zhang, Z.; Zhang, L.; Hedhili, M. N.; Zhang, H.; Wang, P. Plasmonic gold nanocrystals coupled with photonic crystal seamlessly on TiO_2 nanotube photoelectrodes for efficient visible light photoelectrochemical water splitting. *Nano Lett.* **2013**, *13*, 14−20.

(48) Lee, J.; Mubeen, S.; Ji, X.; Stucky, G. D.; Moskovits, M. Plasmonic photoanodes for solar water splitting with visible light. *Nano Lett.* **2012**, *12*, 5014−5019.

(49) Ueno, K.; Misawa, H. Plasmon-enhanced photocurrent generation and water oxidation from visible to near-infrared wavelengths, *NPG Asia Mater.* **2013**, *5*, e61.

(50) Li, J.; Cushing, S. K.; Zheng, P.; Meng, F.; Chu, D.; Wu, N. Plasmon-induced photonic and energy-transfer enhancement of solar water splitting by a hematite nanorod array. *Nat. Commun.* **2013**, *4*, 2651.

(51) Ernst, K.; Belaidi, A.; Konenkamp, R. Solar cell with extremely thin absorber on highly structured substrate. *Semicond. Sci. Technol.* **2003**, *18*, 475−479.

(52) Grätzel, M. Mesoscopic solar cells for electricity and hydrogen production from sunlight. *Chem. Lett.* **2005**, *34*, 8−13.

(53) Yu, Z.; Raman, A.; Fan, S. Fundamental limit of nanophotonic light trapping in solar cells. *Proc. Natl. Acad. Sci* **2010**, *41*, 17491−17496.

(54) Hwang, Y. J.; Wu, C. H.; Hahn, C.; Jeong, H. E.; Yang, P. Si/InGaN core/shell hierarchical nanowire arrays and their photoelectrochemical properties. *Nano Lett.* **2012**, *12*, 1678−1682.

(55) Dotan, H.; Kfir, O.; Sharlin, E.; Blank, O.; Gross, M.; Dumchin, I.; Ankonina, G.; Rothschild, A. Resonant light trapping in ultrathin films for water splitting. *Nat. Mater.* **2013**, *12*, 158.

(56) Sivula, K.; Formal, F. L.; Grätzel, M. WO_3-Fe_2O_3 photo anodes for water splitting: a host scaffold, guest absorber approach. *Chem. Mater.* **2009**, *21*, 2862−2867.

(57) Gardner, R. F. G.; Moss, R. L.; Tanner, D. W. The electrical properties of alpha ferric oxide containing magnesium. *Br. J. App. Phys.* **1966**, *17*, 55−61.

(58) Warnes, B. M.; Aplan, F. F.; Simkovich, G. Electrical conductivity and Seebeck voltage of iron(III) oxide pure and doped, as a function of temperature and oxygen pressure. *Solid State Ionics* **1984**, *12*, 271−276.

(59) Klahr, B. M.; Martinson, A. B. F.; Hamann, T. W. Photoelectrochemical investigation of ultra thin film iron oxide solar cells prepared by atomic layer deposition. *Langmuir* **2011**, *27*, 461−468.

(60) Ma, Y.; Johnson, P. D.; Wassdahl, N.; Guo, J.; Skytt, P.; Nordgren, J.; Kevan, S. D.; Rubensson, J.-E.; Böske, T.; Eberhardt, W. Electronic structures of α-Fe_2O_3 and Fe_3O_4 from O K-edge absorption and emission spectroscopy. *Phys. Rev. B* **1993**, *48*, 2109.

(61) Galuza, A. I.; Beznosov, A. B.; Eremenko, V. V. Optical absorption edge in Fe_2O_3: the exciton-magnon structure. *Low Temp. Phys.* **1998**, *24*, 726.

(62) Velev, J.; Bandyopadhyay, A.; Butler, W. H.; Sarker, S. Electronic and magnetic structure of transition-metal-doped a-hematite. *Phys. Rev. B* **2005**, *71*, 205208.

(63) Liao, P.; Toroker, M. C.; Carter, E. A. Electron transport in pure and doped hematite. *Nano Lett.* **2011**, *11*, 1775−1781.

(64) Liao, P.; Carter, E. A. Hole transport in pure and doped hematite. *J. Appl. Phys.* **2012**, *112*, 013701.

(65) Braun, A.; Sivula, K.; Bora, D. K.; Zhu, J.; Zhang, L.; Grätzel, M.; Guo, J.; Constable, E. C. Direct observation of two electron holes in a hematite photoanode during photoelectrochemical water splitting. *J. Phys. Chem. C* **2012**, *116*, 16870−16875.

(66) Jeong, S.; McDowell, M. T.; Cui, Y. Low-temperature self-catalytic growth of tin oxide nanocones over large areas. *ACS Nano* **2011**, *5*, 5800−5807.

(67) Wang, K. X.; Yu, Z.; Liu, V.; Cui, Y.; Fan, S. Absorption enhancement in ultra thin crystalline silicon solar cells with antireflection and light-trapping nanocone gratings. *Nano Lett.* **2012**, *12*, 1616−1619.

(68) Liu, V.; Fan, S. S^4: a free electromagnetic solver for layered periodic structures. *Comput. Phys. Commun.* **2012**, *183*, 2233−2244.

(69) COMSOL Multiphysics, www.comsol.com.

(70) Palik, E. D. *Handbook of Optical Constants of Solids*; Academic Press: New York, 1985.

(71) Collaboration: Authors and editors of the volumes III/17G-41D. *Hematite (alpha-Fe_2O_3): Optical Properties, Dielectric Constants*. Madelung, O., Rossler, U., Schulz, M., Eds.; SpringerMaterials - The Landolt-Bornstein Database (http://www.springermaterials.com). DOI: 10.1007/10681735_552.

(72) Kim, H.; Horwitz, J. S.; Kushto, G.; Pique, A.; Kafafi, Z. H.; Gilmore, C. M.; Chrisey, D. B. Effect of film thickness on the properties of indium tin oxide thin films. *J. Appl. Phys.* **2000**, *88*, 6021.

(73) Guo, E.-J.; Guo, H.; Lu, H.; Jin, K.; He, M.; Yang, G. Structure and characteristics of ultrathin indium tin oxide films. *Appl. Phys. Lett.* **2011**, *98*, 011905.

(74) Lin, Y.; Xu, Y.; Mayer, M. T.; Simpson, Z. I.; McMahon, G.; Zhou, S.; Wang, D. Growth of p-type hematite by atomic layer deposition and its utilization for improved solar water splitting. *J. Am. Chem. Soc.* **2012**, *134*, 5508−5511.

(75) Hagglund, C.; Zeltzer, G.; Ruiz, R.; Thomann, I.; Lee, H.-B.-R.; Brongersma, M. L.; Bent, S. F. Self-assembly based plasmonic arrays tuned by atomic layer deposition for extreme visible light absorption. *Nano Lett.* **2013**, *13*, 3352−3357.

(76) Fleischer, M.; Weber-Bargioni, A.; Cabrini, S.; Kern, D. P. Fabrication of metallic nanocones by induced deposition of etch masks and ion milling. *Microelectron. Eng.* **2011**, *88*, 2247−2250.

(77) Joo, Y.-H.; Woo, J.-C.; Choi, K.-R.; Kim, H.-S.; Wi, J.-H.; Kim, C.-I. Dry etching of ITO thin films by the addition of gases in Cl_2/BCl_3 inductivity coupled plasma. *Trans. Electr. Electron. Mater.* **2012**, *13*, 157−161.

(78) Wang, S.; Weil, B. D.; Li, Y.; Wang, K. X.; Garnett, E.; Fan, S.; Cui, Y. Large-area free-standing ultrathin single-crystal silicon as processable materials. *Nano Lett.* **2013**, *13*, 4393−4398.

(79) Cai, J.; Chen, S.; Hu, J.; Wang, Z.; Ma, Y.; Qi, L. Top-down fabrication of hematite mesocrystals with tunable morphologies. *CrystEngComm* **2013**, *15*, 6284.

(80) Cesar, I.; Kay, A.; Martinez, J. A. G.; Gratzel, M. Translucent thin film Fe_2O_3 photoanodes for efficient water splitting by sunlight: nanostructure-directing effect of Si-doping. *J. Am. Chem. Soc.* **2006**, *128*, 4582−4583.

(81) Cesar, I.; Sivula, K.; Kay, A.; Zboril, R.; Grätzel, M. Influence of feature size, film thickness, and silicon doping on the performance of nanostructured hematite photoanodes for solar water splitting. *J. Phys. Chem. C* **2009**, *113*, 772−782.

(82) Chen, Z.; Cummins, D.; Reinecke, B. N.; Clark, E.; Sunkara, M. K.; Jaramillo, T. F. Core-shell MoO_3-MoS_2 nanowires for hydrogen evolution: a functional design for electrocatalytic materials. *Nano Lett.* **2011**, *11*, 4168−4175.

(83) Chen, Z.; Forman, A. J.; Jaramillo, T. F. Bridging the gap between bulk and nano structured photoelectrodes: the impact of surface states on the electrocatalytic and photoelectrochemical properties of MoS_2. *J. Phys. Chem. C* **2013**, *117*, 9713−9722.